Front. Optoelectron. 2014, 7(3): 320–337
DOI 10.1007/s12200-014-0469-4

REVIEW ARTICLE

# A review of recent progress in plasmon-assisted nanophotonic devices

**Jian WANG (✉)**

Wuhan National Laboratory for Optoelectronics, School of Optical and Electronic Information, Huazhong University of Science and Technology, Wuhan 430074, China



**Abstract** Plasmonics squeezes light into dimensions far beyond the diffraction limit by coupling the light with the surface collective oscillation of free electrons at the interface of a metal and a dielectric. Plasmonics, referred to as a promising candidate for high-speed and high-density integrated circuits, bridges microscale photonics and nanoscale electronics and offers similar speed of photonic devices and similar dimension of electronic devices. Various types of passive and active surface plasmon polariton (SPP) enabled devices with enhanced deep-subwavelength mode confinement have attracted increasing interest including waveguides, lasers and biosensors. Despite the trade-off between the unavoidable metal absorption loss and extreme light concentration, the ever-increasing research efforts have been devoted to seeking low-loss plasmon-assisted nanophotonic devices with deep-subwavelength mode confinement, which might find potential applications in high-density nanophotonic integration and efficient nonlinear signal processing. In addition, other plasmon-assisted nanophotonic devices might also promote grooming functionalities and applications benefiting from plasmonics.

In this review article, we give a brief overview of our recent progress in plasmon-assisted nanophotonic devices and their wide applications, including long-range hybrid plasmonic slot (LRHPS) waveguide, ultra-compact plasmonic microresonator with efficient thermo-optic tuning, high quality ($Q$) factor and small mode volume, compact active hybrid plasmonic ring resonator for deep-subwavelength lasing applications, fabricated hybrid plasmonic waveguides for terabit-scale photonic interconnection, and metamaterials-based broadband and selective generation of orbital angular momentum (OAM) carrying vector beams. It is believed that plasmonics opens possible new ways to facilitate next chip-scale key devices and frontier technologies.

**Keywords** plasmonics, surface plasmon polariton (SPP), nanophotonic devices, plasmonic waveguide, photonic interconnection, metamaterials

Received July 12, 2014; accepted July 25, 2014

E-mail: jwang@hust.edu.cn

## 1 Introduction

"Plasmonics" is termed as a flourishing new device technology for deep-subwavelength light concentration and fast information manipulation [1]. Plasmonics has the potential to increase the processing speed and shrink the device dimension of future integrated circuits [2–5]. The importance and the key role of plasmonics are illustrated in Fig. 1, showing the operation speed and critical device dimension of different chip-scale device technologies [2]. In the past, the operation speed is slow and the device is bulky. Electronic devices benefit from mature semiconductor industry with their volumes scaled down to nanscale dimensions. However, it is a great challenge to achieve fast purely electronic circuits operating above 10 GHz due to electronic interconnection delay time issues. Photonic devices facilitate high operation speed and possess a large data-carrying capacity owing to the huge photonic bandwidth. Nevertheless, dielectric photonic devices have great limitations in their dimensions because of the unavoidable diffraction effects, resulting in difficult scaling of photonic devices as electronic ones. Remarkably, plasmonics bridges microscale photonics and nanoscale electronics. Plasmonics offers the combined advantages from both the device dimension of electronics and the operation speed of photonics. Plasmonic devices, featuring similar speed of photonic devices and similar dimension of electronic devices, are therefore referred to as potential promising candidates for high-speed and high-density integrated circuits.

Conductors, e.g., metallic components, especially metal nanostructures, are right plasmonic devices tackling the existing issues of photonics or electronics and offering combined advances of photonic and electronic properties. The metals widely employed in traditional electronic interconnections such as Cu and Al, also provide possible excitation of surface plasmon polaritons (SPPs). It is believed that SPPs are electromagnetic waves coupled to surface collective oscillations of free electrons in metal and propagating along a metal-dielectric interface [6–13]. Such unique feature implies that SPP can break down the diffraction limit of conventional optics and lead to deep-subwavelength confinement [3,9,11]. SPP-based devices offer similar huge bandwidth of information processing as in conventional dielectric-based photonic devices and yet not diffraction limited. Recently, various types of passive and active SPP-based devices with enhanced deep-subwavelength mode confinement such as waveguides, lasers and biosensors have attracted increasing interest [14–19]. Unfortunately, the existence of metal material in SPP-based devices brings a relatively large absorption loss when compared to pure dielectric nanophotonic devices (e.g., silicon waveguides). Generally speaking, there exists a trade-off between the absorption loss and mode confinement. So far, the ever-increasing research efforts have been devoted to looking for low-loss SPP-based waveguides with deep-subwavelength mode confinement. Typical examples include long-range dielectric-metal-dielectric (DMD) plasmonic waveguide, hybrid plasmonic waveguide, and long-range hybrid plasmonic waveguide [20–30]. These plasmonic waveguides open possible ways to facilitate simultaneous tight light confinement and low propagation loss, which might find potential applications in high-density nanophotonic integration and efficient nonlinear signal processing. Additionally, other plasmon-assisted nanophotonic devices might also promote grooming functionalities and applications benefiting from plasmonics.

In this review article, we go over our recent progress in plasmon-assisted nanophotonic devices and their applications, including long-range hybrid plasmonic slot (LRHPS) waveguide [31], ultra-compact plasmonic microresonator with efficient thermo-optic tuning, high quality ($Q$) factor and small mode volume [32], compact active hybrid plasmonic ring resonator for deep-subwavelength lasing applications [33], fabricated hybrid plasmonic waveguides for terabit-scale photonic interconnection [34], and metamaterials-based broadband and selective generation of orbital angular momentum (OAM) carrying vector beams [35,36].

## 2 Surface plasmon polaritons (SPPs)

SPPs, also known as surface plasmons (SPs), are widely recognized in the field of surface science [37]. As illustrated in Fig. 2, SPPs can be regarded as two-dimensional bound electromagnetic excitations propagating along the interface of a dielectric ($\varepsilon_d$) and a conductor, usually a metal ($\varepsilon_m$). SPPs are essentially light waves trapped on the interface as a result of the interaction between the light waves and free electrons of the metal. The electromagnetic fields of light waves cause in-resonance surface collective oscillations of free electrons. Such resonant interaction between light waves and surface charge oscillations forms SPPs featuring unique properties. It is noted that the generation of surface charge requires an electric field normal to the surface. Hence, one can excite a surface transverse magnetic (TM) polarized electromagnetic field, i.e., polarized in the propagation plane. The electric field component perpendicular to the surface peaks at the interface and decays exponentially away into both of the two side media (i.e., dielectric and metal). The electric field in the perpendicular direction is evanescent with non-radiative nature which prevents power from propagating away from the surface. In the dielectric, typically air or glass, the field decay length ($\delta_d$) is on the order of half the light wavelength. In the metal, the field decay length into the metal ($\delta_m$) is dependent on the skin depth. In contrast, it is clear that the transverse electric (TE) polarized electromagnetic field, i.e., polarized perpendicular to the propagation plane, cannot be coupled to the longitudinal oscillations of free electrons in metals to form SPPs [6].

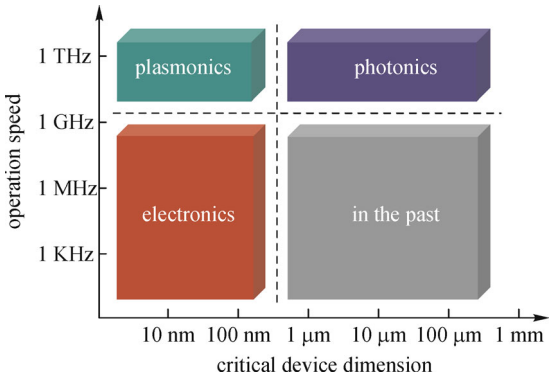


**Fig. 1** Typical operation speed and critical device dimension of different chip-scale device technologies (plasmonics, photonics, electronics and the past)

In addition to SPP as one kind of surface science at the interface between a metal and a dielectric, another kind of surface science could be also at the interface between two different dielectrics, especially one low-index dielectric ($\varepsilon_{dL}$) and one high-index dielectric ($\varepsilon_{dH}$). There exists significant discontinuity of electric field at the high-contrast-index dielectric-dielectric interface. Remarkably, surface science provides an alternative approach to forming waveguides beyond previous well known waveguides guiding modes in the high-index dielectric. As depicted in Fig. 3, different and flexible combinations of high-contrast-index dielectric-dielectric interfaces and

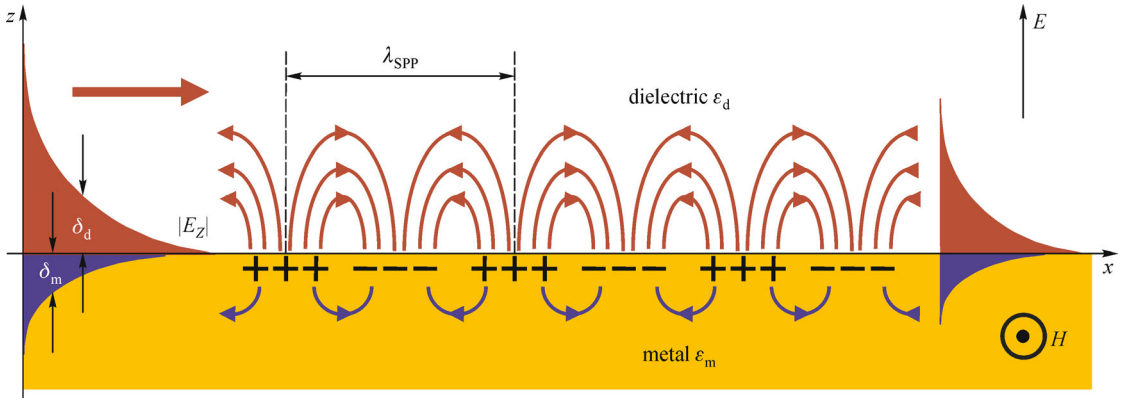


**Fig. 2** Schematic illustration of field distribution of surface plasmon polariton (SPP) at the interface between a conductor (metal) and a dielectric

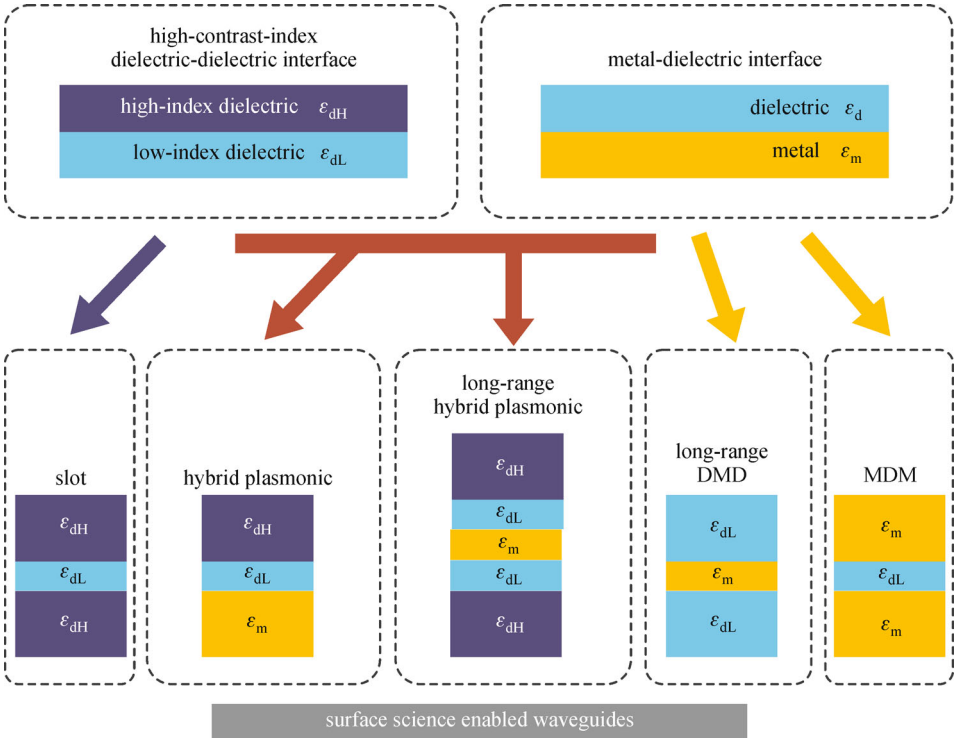


**Fig. 3** Illustration of surface science enabled waveguides (slot, hybrid plasmonic, long-range hybrid plasmonic, long-range DMD, MDM) with their super modes hybridized from the surface modes at the high-contrast-index dielectric-dielectric interface or/and at the metal-dielectric interface. DMD: dielectric-metal-dielectric; MDM: metal-dielectric-metal

metal-dielectric interfaces give birth to various waveguide structures. For instance, 1) two high-contrast-index dielectric-dielectric interfaces form a slot waveguide with the electric field greatly enhanced and confined in the low-index slot region [38]; 2) two metal-dielectric interfaces form long-range DMD waveguide or metal-dielectric-metal (MDM) waveguide; 3) one high-contrast-index dielectric-dielectric interface and one metal-dielectric interface form hybrid plasmonic waveguide; 4) two high-contrast-index dielectric-dielectric interfaces and two metal-dielectric interfaces form a long-range hybrid plasmonic waveguide. Those new waveguides benefiting from surface science have gained increasing interest in recent years.

## 3 Long-range hybrid plasmonic slot (LRHPS) waveguide [31]

Figure 4 shows the proposed LRHPS waveguide consisting of a silica substrate, two high-index silicon (Si) strips, two low-index silicon nanocrystal (Si-nc) slots and a metal.

The vertical area between the two high-index Si strips is filled with a sandwiched DMD structure. The metal is a thin silver (Ag) film with a width of $W_{Ag}$ and dielectrics are low-index (compared to silicon) dielectrics. Here, we choose the low-index dielectrics as Si-nc which is a highly nonlinear material at the telecommunication wavelength. All these metallic and dielectric parts on the silica substrate have the same height of $H_{WG.}$ The width of each Si strip and Si-nc slot is $W_{Si}$ and $W_{Si\text{-}nc}$, respectively. The silica substrate has a height of $H_{Silica}$. The mode of the designed waveguide is expected to be highly confined and guided in the two nano-scale low-index Si-nc slots.

To comprehensively understand the origin, principle and advantages of the designed LRHPS waveguide, we start from the well-known long-range surface plasmon polariton waveguide and slot waveguide as follows.

1) Figure 5(a) shows the typical structure of a long-range surface plasmon polariton waveguide, which has a thin metal strip with a width of $W_{Ag}$ (silver) bounded by symmetric dielectric claddings (Si-nc). Such a DMD-structured (Si-nc-silver-Si-nc) waveguide supports two distinct modes, i.e., symmetric bound ($s_b$) mode and asymmetric bound ($a_b$) mode. Figure 5(b) depicts the main transverse electric field component $E_x$ of the $s_b$ mode, which has a symmetric profile across the structure (along the $x$-direction). The corresponding charge density in the thin metal has an asymmetric distribution over the metal width $W_{Ag}$. Hence, low absorption loss or long propagation range is expected due to less mode penetration into the metal. In contrast, Fig. 5(c) plots the $a_b$ mode which has an asymmetric profile of $E_x$ accompanied by a symmetric distribution of charge density over the structure, resulting in a large absorption loss and short propagation range. Consequently, the $s_b$ and $a_b$ modes are referred to as long-range and short-range surface plasmon polariton modes, respectively. Remarkably, it can be clearly seen from Figs. 5(b) and 5(c) that the main transverse electric field component $E_x$ of both $s_b$ and $a_b$ modes has a relatively slow decay speed into the surrounding dielectrics. Additionally, one can also see that a considerable proportion of mode energy spreads in the dielectric areas, corresponding to a relatively large mode area.

2) In DMD-structured waveguides, the modes are extended to the surrounding dielectrics without any extra constrains and the main transverse electric field $E_x$ remains a high value at a remarkable distance away from the interface of metal and dielectric claddings. To avoid the mode dissipating too much away from the interface, a laudable goal is to confine the mode field within a small dielectric region near the interface. Fortunately, slot waveguide provides a possible solution [38]. Shown in Figs. 5(d) and 5(e) are a typical structure and field distribution of a vertical slot waveguide comprising a low-index slot (e.g., Si-nc) bounded by two high-index slabs (e.g., Si) on a silica substrate. Due to the discontinuity of electric field at the interface between two dielectric materials (e.g., Si-nc and Si) with a high-index contrast, the electric field can be greatly enhanced and confined in the low-index slot region [38,39]. It is believed that the recently reported hybrid plasmonic waveguide follows a similar idea to slot waveguide [38]. The hybrid mode is confined in the low-index slot region bounded by a high-index material and a metal. Although the mode field is confined more tightly compared to the DMD structure, the mode propagation range of the hybrid plasmonic waveguide is shorter than the long-range surface plasmon polariton mode of the DMD structure.

3) Both long-range surface plasmon polariton waveguide (DMD structure) and hybrid plasmonic waveguide can be regarded as two variations (two interfaces) of traditional single-interface plasmonic waveguide. The former introduces a second metal-dielectric interface to reduce absorption loss and extend propagation range, while the latter adds a high-index-contrast dielectric-dielectric interface to enhance the mode confinement. By combining the advantages of long-range surface plasmon polariton waveguide and hybrid plasmonic waveguide or slot waveguide, it is possible to form a LRHPS waveguide

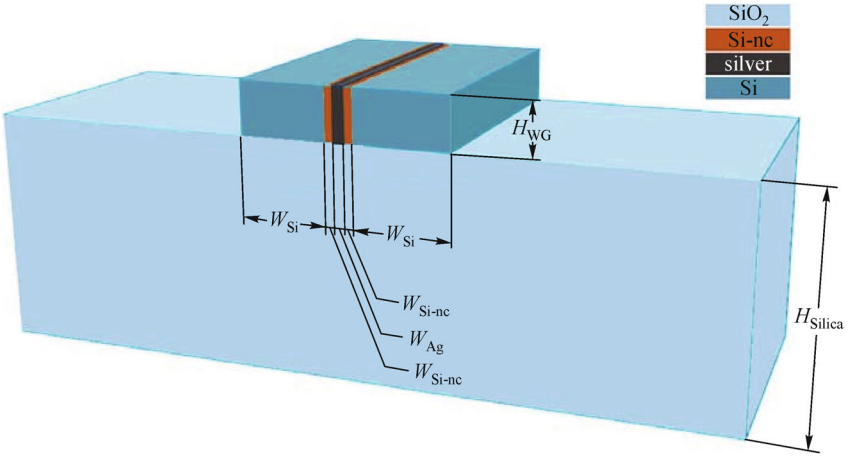


**Fig. 4** Schematic illustration of 3-D structure of the long-range hybrid plasmonic slot (LRHPS) waveguide [31]

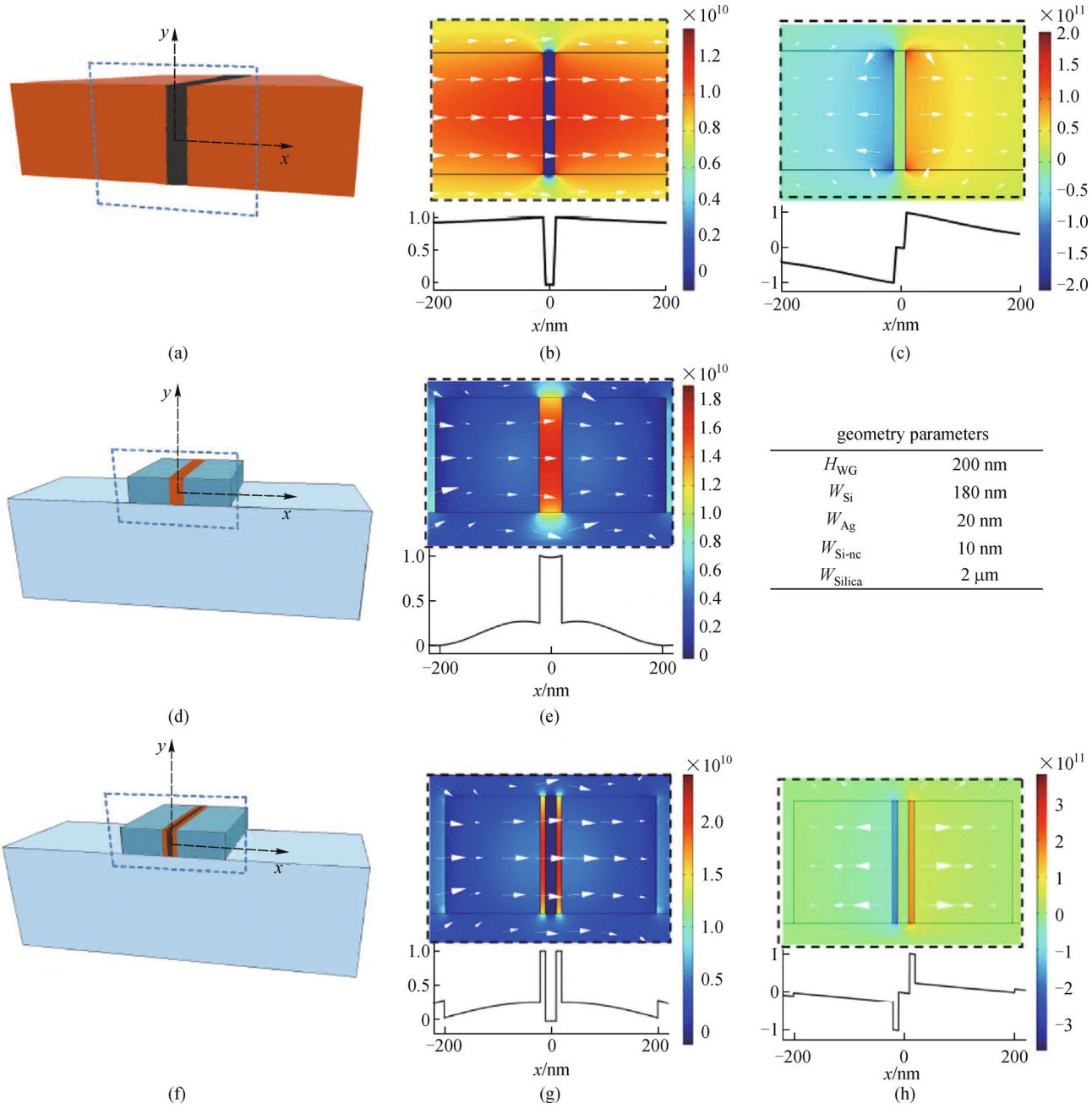


| geometry parameters | |
|---|---|
| $H_{WG}$ | 200 nm |
| $W_{Si}$ | 180 nm |
| $W_{Ag}$ | 20 nm |
| $W_{Si\text{-}nc}$ | 10 nm |
| $W_{Silica}$ | 2 μm |

**Fig. 5** Schematic structures of (a) traditional dielectric-metal-dielectric (DMD) waveguide, (d) vertical slot waveguide, (f) proposed long-range hybrid plasmonic slot (LRHPS) waveguide, and distributions of main transverse electric field component $E_x$ for (b) long-range surface plasmon polariton (SPP) mode and (c) short-range SPP mode of DMD waveguide, (e) vertical slot mode of vertical slot waveguide, (g) long-range hybrid (LRH) mode and (h) short-range hybrid (SRH) mode of LRHPS waveguide. The curves sketched in (b), (c), (e), (g) and (h) show the $E_x(x,0)$ distribution in the waveguides. The arrows plotted in the mode field represent the direction and relative amplitude of transverse electric field component $E_x$ [31]

enabling a millimeter-scale propagation range together with a deep-subwavelength mode confinement. As depicted in Fig. 5(f), two high-index strips (e.g., Si) are added as outer claddings of a traditional vertical DMD-structured (e.g., Si-nc-silver-Si-nc) waveguide on a silica substrate. Similar to Figs. 5(b) and 5(c), the LRHPS waveguide also supports one $s_b$ mode and one $a_b$ mode, as shown in Figs. 5(g) and 5(h), respectively. According to the distribution of the electric field and charge density, it is expected that the $s_b$ mode has a low absorption loss and long propagation range while the $a_b$ mode has a large absorption loss and short propagation range. We call $s_b$ mode in Fig. 5(g) and $a_b$ mode in Fig. 5(h) as long-range hybrid (LRH) mode and short-range hybrid (SRH) mode,

respectively. In addition, as shown in Figs. 5(g) and 5(h), at the interface of Si-nc and Si, the main transverse electric field component $E_x$ is discontinuous and a high power density is obtained in the two nano-scale low-index Si-nc slots separated by a thin metal film. Hence, deep-subwavelength tight mode confinement can be also achieved benefiting from the added two high-index Si claddings. As a consequence, the LRH mode of LRHPS waveguide, as shown in Fig. 5(h), can potentially provide a deep-subwavelength mode confinement accompanied by a long propagation range on the scale of millimeter. The LRH mode and SRH mode are both TE-like modes as high-index slab (Si), low-index slot (Si-nc) and metal film (silver) are aligned along the horizontal direction. We calculate the mode distribution of different waveguide structures in Fig. 5 using finite-element method software package COMSOL Multiphysics. For the traditional DMD waveguide shown in Figs. 5(a) – 5(c), the slot width equals the sum of $W_{Ag}$ and $W_{Si\text{-}nc}$, while the waveguide height is $H_{WG}$. The Si-nc slot region in Figs. 5(d) and 5(e) has the same size as the sum of the silver and two Si-nc slots in Fig. 5(f). Detailed geometry parameters are listed in the inset of Fig. 5. The refractive indices of each material at 1550 nm are $n_{Ag} = 0.1453 + 11.3587i$ [22], $n_{Silica} = 1.445$, $n_{Si} = 3.455$ and $n_{Si\text{-}nc} = 1.723$ [40].

To further characterize the properties of LRH and SRH modes, we plot in Fig. 6 the normalized phase and attenuation constants of the LRH and SRH modes as a function of the metal width. The normalized phase and attenuation constants are corresponding to the real and imaginary parts of the calculated effective mode index. Here, $\beta_0 = 2\pi/\lambda$ is the phase constant of light ($\lambda$ is wavelength) in the vacuum and the mode effective index is $n_{eff} = \beta/\beta_0 + \alpha/\beta_0$. One can see that the metal width plays an important role leading to unique features of LRH and SRH modes. When the metal film is thin, LRH and SRH modes show distinct phase and attenuation properties. In particular, the LRH mode has much lower attenuation than the SRH mode. When reducing the metal width, the attenuation of the LRH mode decreases with its mode field increasingly expelled from the metal and entering more deeply into the Si-nc slots, while the SRH mode features increasing penetration into the metal and resultant absorption loss. For a large metal width, the LRH and SRH modes are almost degenerate with the mode of the conventional hybrid plasmonic waveguide which has a metal (silver), low-index slot (Si-nc) and high-index strip (Si) from left to right on a silica substrate. The normalized phase and attenuation constants of the degenerate mode are also depicted in Fig. 6 as the dotted lines for reference.

Propagation length is an important parameter describing the mode feature in a plasmonic waveguide. The imaginary part of the effective mode index ($\mathrm{Im}(n_{eff})$) indicates the loss property of the mode. The propagation length of mode ($L_{prop}$), defined as the distances from the input to where the mode field decays by a factor of 1/e [41], is calculated by

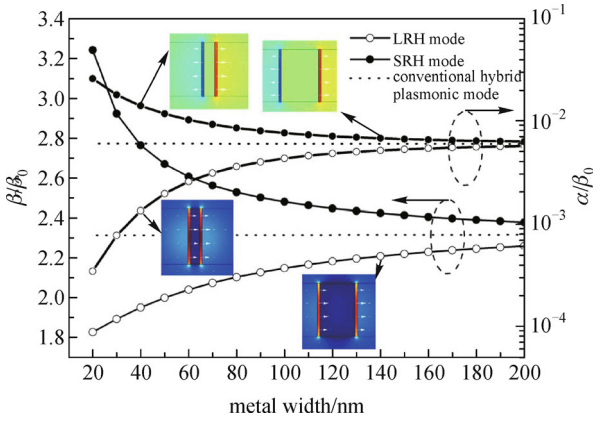


**Fig. 6** Normalized phase and attenuation constants of the long-range hybrid (LRH) and short-range hybrid (SRH) modes of long-range hybrid plasmonic slot (LRHPS) waveguide. The dotted line corresponds to a conventional hybrid plasmonic waveguide (a silver, a Si-nc slot and a Si strip from left to right on a silica substrate) with a metal width of 300 nm [31]

$L_{prop} = \lambda/(4\pi \cdot \mathrm{Im}(n_{eff}))$. And the corresponding waveguide loss could be obtained by $\alpha = -10\log(1/e)/L_{prop} \approx 4.343/L_{prop}$. It is evident that the LRH mode has a smaller imaginary part of $n_{eff}$ and a resultant longer propagation length compared to the SRH mode. Another two parameters known as normalized power and intensity are of great importance showing the ability of mode confinement. Nonlinearity is also a key parameter when using plasmonic waveguide in nonlinear optical signal processing applications. Si-nc has a large nonlinear refractive index $n_2$ at the telecommunication wavelength. The reported $n_2$ can be as high as $4 \times 10^{-13}$ cm$^2$/W under a silicon excess of 0.08, an annealing temperature of 800°C, and a deposition method of plasma enhanced chemical vapor deposition (PECVD) [42]. Chromatic dispersion is regarded as another key parameter for wideband operation in optical communication applications. The chromatic dispersion is calculated by the expression $D = -\lambda/c \cdot d^2[\mathrm{Re}(n_{eff})]/d\lambda^2$.

We further study the geometry-dependence of the propagation length of the LRH mode, normalized power and intensity of LRH and SRH modes as a function of slot width under different values of metal width, the nonlinearity of LRH and SRH modes as functions of slot width and wavelength under a set of geometry parameters, the wavelength dependence of the chromatic dispersion and dispersion slope for LRH and SRH modes within a wavelength range from 1500 to 1600 nm. More details of the obtained results and discussion can be found in Ref. [31].

## 4 Ultra-compact plasmonic microresonator [32]

Resonators at micro/nano scale have seen wide applica-

tions ranging from light sources, passive on-chip photonic elements, biosensing, and so on [43]. Specifically, when the resonance can be tuned (e.g., electric-optic, thermo-optic, Kerr effect, etc.), resonators can be more flexible and functional. Meanwhile, for a resonator, it is advantageous to reduce its footprint, which is beneficial for its integration with other components. Plasmonics are promising candidates in the miniaturization and functionality improvement of resonators, since the mode energy can be tightly confined at the interface of metal and dielectric capable of breaking the diffraction limit [11]. Moreover, this tightly confined mode can increase the light-matter interaction, which offers a lot of opportunities for more efficient resonance tuning and control.

We design a new type of plasmonic resonator consisting of a ZnO ring on a silver substrate, as depicted in Fig. 7(a). The inset depicts the cross-section of the resonator, where a hexagonal shape of the ZnO can be seen. SPP can be supported at the interface of the ZnO and silver substrate. Due to the circular geometrical structure, this SPP can form a whispering-gallery-like wave. This kind of whispering-gallery-like mode can be characterized by an azimuthal mode number $M$, which determines the number of mode field maxima in a round trip. We show in Fig. 7(b) the energy density distribution at the cross-section view each with a resonance in the 630 nm band under four sets of geometrical parameters. The simulation is based on a full-vector finite-element method [44]. The silver is modeled by a Drude model (fitting the Johnson and Christy's experimental data [45]) and ZnO's permittivity is obtained from a Sellmeier equation [46]. This mode is similar to the plasmon mode supported by a dielectric loaded surface plasmon polariton (DLSPP) waveguide in spite of the ring-resonator structure [47]. Different from the straight waveguide, the whispering-gallery-like mode will slightly extend outwards due to the bending radiation, which can also be seen from the contour of the mode energy density shown in Fig. 7(b).

For a resonator, $Q$ factor and mode volume ($V$) are two key parameters. The designed resonator can simultaneously maintain ultra-small mode volume (~0.01 μm$^3$) and relatively high quality factor (~350). Furthermore, the simulation results show that due to the large thermo-optic coefficient (TOC) of ZnO and silver, the resonance of the whispering-gallery-like modes can be efficiently tuned by temperature control. More details of the obtained results and discussion can be found in Ref. [32].

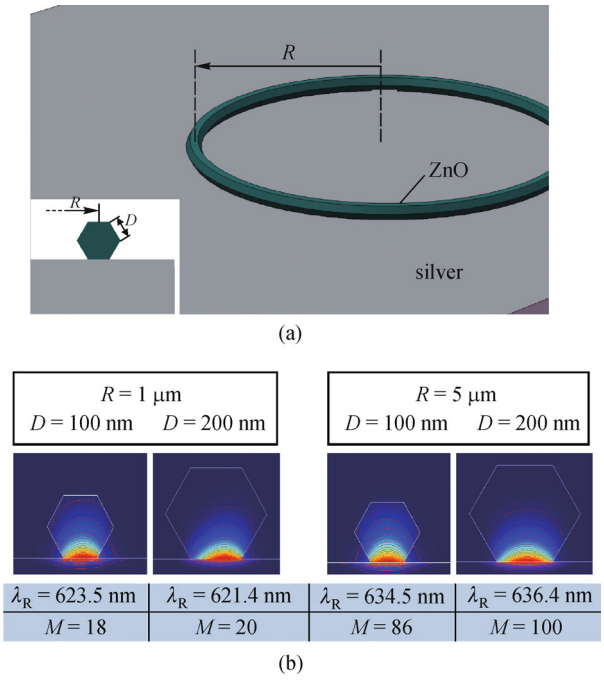


**Fig. 7** (a) 3D structure illustration of the designed plasmonic microresonator; (b) energy density distribution and contour plot under certain geometrical parameters [32]

## 5 Active hybrid plasmonic ring resonator for deep-subwavelength lasing [33]

SPP holds great potential to break the diffraction limit and shows interesting and wide applications, where light can be generated and controlled at deep-subwavelength scale [11]. SPP-assisted light emitters have gained more and more interest thanks to its ability of confining light field within an ultra-small area ($<(\lambda/2n)^3$). Typical SPP-based light emitters include metal-cavity shield laser [48] and surface plasmon amplification by stimulated emission of radiation (SPASER) based nanolaser [49]. It is noted that high gain is always desired in SPP-assisted lasers to compensate the absorption loss for successful lasing due to metallic absorption loss. Recently, a hybrid plasmonic waveguide was designed in order to reduce the absorption loss while still preserving a strong mode confinement [15,17]. A plasmon laser was then proposed and demonstrated in the experiment when incorporating a semiconductor nanowire [18]. Remarkably, in this kind of plasmon laser, the feedback mechanism relies on a Fabry-Pérot cavity. The two end-facets of the semiconductor nanowire offer the refection and feedback which are necessary for lasing applications. However, limited $Q$ factor is achieved in this structure due to small reflectivity and mirror loss. It is expected that round-trip whispering-gallery cavity might increase the $Q$ factor and improve the performance [50], while so far there has been limited research efforts to lasing applications using whispering-gallery cavity.

We design a simple active hybrid plasmonic ring resonator supporting whispering-gallery-like hybrid plasmonic modes. Figure 8(a) shows typical structure of the proposed active hybrid plasmonic ring resonator. The key component of the structure is a semiconductor nanowire with a circular cross section (radius $R_c$) which is designed in a ring shape with a radius of $R_r$. The ring shaped semiconductor nanowire is put on a thin low-index

dielectric layer placed on top of a metal substrate. Shown in Fig. 8(b) is the cross section view, in which one can clearly see that a gap region (low-index dielectric layer) with a height of $H_g$ is formed between the semiconductor nanowire and the metal substrate. In the designed structure, cadmium sulfide (CdS), magnesium floride ($MgF_2$), and silver (Ag) are chosen as the semiconductor nanowire, the low-index dielectric layer, and the metal substrate, respectively. The supported mode distribution at the lasing wavelength of CdS semiconductor nanowire (~490 nm) is calculated. Drude model is used to model silver in the simulations and the permittivities of CdS and $MgF_2$ are 5.76 and 1.96, respectively [18,45].

Remarkably, two major modes are supported in the designed hybrid plasmonic structure. One is called hybrid plasmonic (HP) mode and the other is known as fundamental photonic (PH) mode. We can consider the HP mode as a supermode. The mechanism of such kind of supermode relies on the combined contributions from both SPP and discontinuity of electric fields at the interface between the high-index semiconductor nanowire (CdS) and low-index dielectric gap layer ($MgF_2$). Alternatively, the HP mode is also regarded as the coupling result between the surface plasmon mode and in-phase fundamental photonic mode [51]. The fundamental PH mode is somehow similar to the traditional fundamental mode, which is confined and guided in the high-index material. Beyond HP mode and fundamental PH mode, there exist some other modes possibly supported in the hybrid plasmonic structure. Those modes include: 1) supermode from coupling between the surface plasmon mode and out-of-phase fundamental photonic mode [51]; 2) supermodes from coupling between the surface plasmon mode and high-order photonic modes; 3) high-order photonic modes with large cross section radius of semiconductor nanowire. It is noted that these other modes beyond HP mode and fundamental PH mode are not taken into consideration here for simplicity when the designed structure is optimized to achieve superior performance (e.g., small mode volume with small nanowire cross section radius). This is also reasonable because these modes are more easily cut off and also not of interest for the proposed compact deep-subwavelength lasing applications. Figures 8(c) and 8(d) depict the cross section views of the on-resonance (~490 nm) energy density distributions ($H_g = 10$ nm, $R_c = 100$ nm, $R_r = 800$ nm) for the HP mode and fundamental PH mode, respectively. It can be clearly seen that the HP mode peaks in the low-index gap region and a part of the mode field overlaps with the semiconductor nanowire to offer the gain necessary for lasing applications. This implies that the HP mode shows smaller mode volume together with favorable tolerance to the metal absorption loss. In contrast, the fundamental PH mode is mainly confined in the semiconductor nanowire, featuring a relatively larger mode size and less overlap with the metal substrate. Furthermore, Figs. 8(c) and 8(d) depict the contour plots of the mode energy density. One can clearly see that the energies of both HP and fundamental PH modes slightly extend outwards. Such phenomenon can be ascribed to the bending radiation effect. Note that the gap layer and ring structure in the proposed design play important roles in lasing applications. To further show the

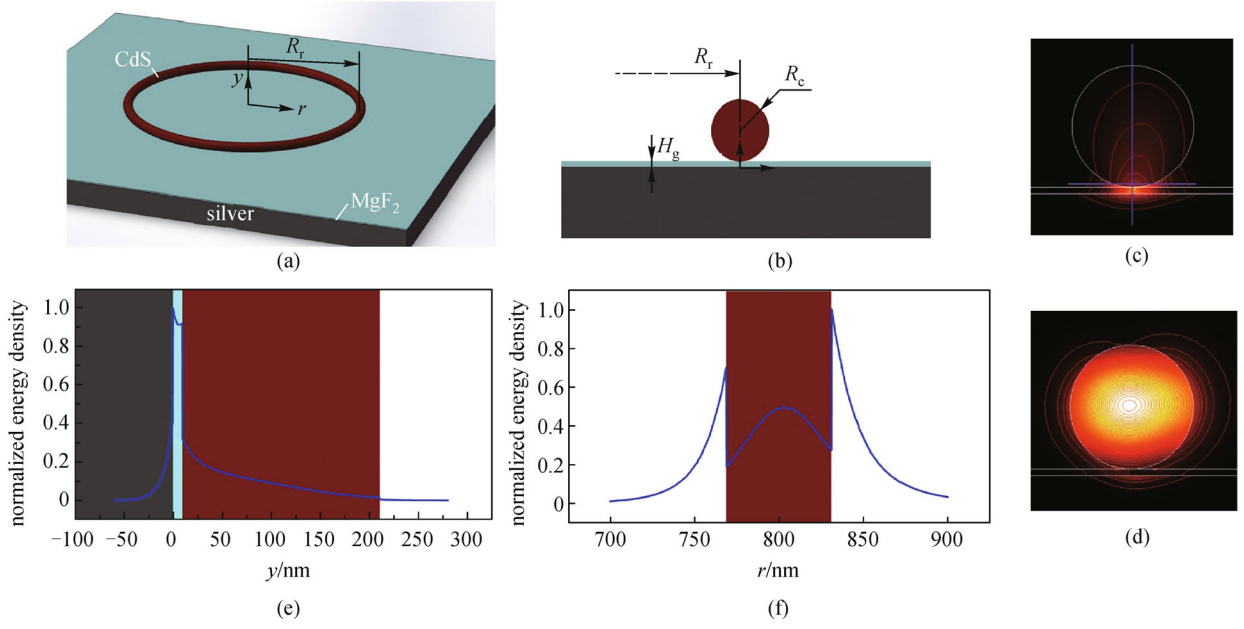


**Fig. 8** (a) Schematic illustration of 3D structure for the designed active hybrid plasmonic ring resonator; (b) cross section of the hybrid plasmonic ring resonator; energy flux density distributions and contour plots for the hybrid plasmonic (HP) mode (c) and fundamental photonic (PH) mode (d); normalized energy flux density for the HP mode along *y* direction (e) and *r* direction (f) [33]

impact of gap layer and ring structure on the HP mode distribution, we calculate and show in Figs. 8(e) and 8(f) the normalized energy density distribution along $y$ ($r$ = 800 nm) and radial ($y$ = 15 nm) directions, which are corresponding to the marked vertical and horizontal blue lines shown in Fig. 8(c), respectively. The mode energy density shows a sharp peak in the low-index gap layer region along the $y$ direction. The mode energy density profile within the semiconductor nanowire region along the radial direction has a Gaussian-like shape with a width of only ~50 nm, which is actually limited by the physical dimension of the semiconductor nanowire along this direction. In particular, for the mode energy density profile at symmetric positions with respect to the center vertical axis of the semiconductor nanowire, the outer branch of the profile close to the outer rim of the ring resonator shows higher energy density, which indicates that more energy is confined at the outward parts of the ring resonator.

It is noted that geometrical parameters can impact on the operation performance of the proposed active hybrid plasmonic ring resonator. Three key geometrical parameters are as follows: 1) height of low-index gap layer ($H_g$); 2) radius of cross section ($R_c$); 3) radius of ring structure ($R_r$). More details of the obtained results and discussion can be found in Ref. [33].

Shown in Fig. 9 is the $Q$ factor and mode volume ($V$) as a function of the gap height for both HP and fundamental PH modes at a resonance within the lasing wavelength band [52] ($R_c$ = 100 nm, $R_r$ = 800 nm). The $Q$ factor increases from 300 to 1650 as increasing the gap height from 5 to 30 nm for the HP mode. This can be explained with the fact that less mode energy is distributed in the silver substrate resulting in lower absorption loss and higher $Q$ factor with the increase of gap height. For the fundamental PH mode, the $Q$ factor also increases with the gap height. We can briefly explain such phenomenon as follows. Less mode energy leaks into the metal substrate as moving the semiconductor nanowire away from the metal substrate, thus the total loss of the ring resonator is reduced, resulting in the increase of the $Q$ factor. Ultra-small (~0.0022 μm$^3$) mode volume is achievable at deep-subwavelength scale under a small gap height of 5 nm due to tight HP mode confinement in the small gap layer region. When increasing the gap height from 5 to 30 nm, it is found that the mode volume changes from 0.0022 to 0.0318 μm$^3$. For the fundamental PH mode, as depicted in Fig. 9, the mode volume remains almost unchanged, i.e., slightly varying from 0.0842 to 0.0884 μm$^3$ as increasing the gap height. It is found from Fig. 9 that the fundamental PH mode features larger mode volume and less dependency of mode volume on the gap layer than the HP mode.

The diffraction limit may have different impacts on the HP mode and fundamental PH mode. Figures 10(a) and 10 (b) depict the properties of the HP mode and fundamental PH mode as a function of the cross section radius $R_c$ of the semiconductor nanowire ($H_g$ = 10 nm, $R_r$ = 800 nm).

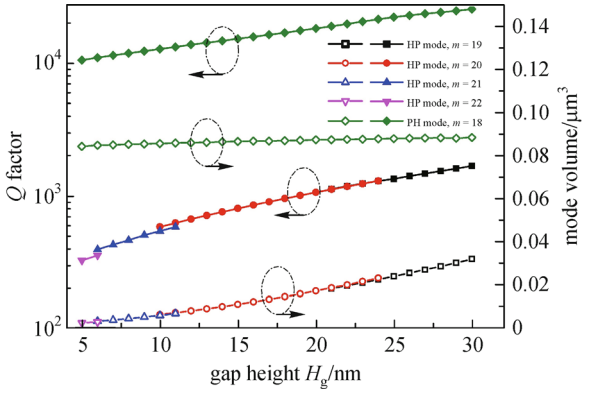


**Fig. 9** Gap height ($H_g$) dependence of the $Q$ factor and mode volume at a resonance in the lasing wavelength band of CdS for the hybrid plasmonic (HP) mode and fundamental photonic (PH) mode ($R_c$ = 100 nm, $R_r$ = 800 nm) [33]

Shown in Fig. 10(a) is the cross section radius ($R_c$) dependent effective refractive index ($n_{eff}$) of the HP mode and fundamental PH mode for different mode numbers with possible resonance within the lasing wavelength band [52]. We can deduce several important conclusions from Fig. 10(a) as follows. 1) One can clearly see a cut-off effective refractive index at ~1.185 for the HP mode and ~1.283 for the fundamental PH mode; 2) It is shown that the fundamental PH mode is cut off when the cross section radius ($R_c$) is smaller than 70 nm. This is because that at such small geometrical dimensions the mode confinement mechanism is broken by the diffraction limit effect for the fundamental PH mode, which causes severe evanescence of the fundamental PH mode at deep-subwavelength scale and prohibits photonic lasing of the fundamental PH mode. The typical cut-off radius is 70 nm, which is slightly larger than the previously reported cut-off radius of 65 nm [52]. This can be ascribed to the bending effect of the semiconductor nanowire ring resonator and the corresponding radiation loss. Remarkably, one can selectively suppress fundamental PH mode lasing and support only HP mode lasing according to the cut-off radius of 70 nm for the fundamental PH mode. That is, both HP mode and fundamental PH mode lasing are available when cross section radius $R_c$ is larger than 70 nm, while only the HP mode lasing is supported when cross section radius $R_c$ is less than 70 nm. 3) Even under an ultra-small cross section radius $R_c$ of 20 nm, the HP mode is still supported, showing its full ability to break the diffraction limit. 4) When reducing the cross section radius $R_c$, it is found that the whispering-gallery-like mode having a smaller azimuthal mode number disappears first for both HP and fundamental PH modes. For example, the mode number of the supported fundamental PH modes follows $m \geqslant 8$ at $R_c$ = 130 nm and $m \geqslant 13$ at $R_c$ = 75 nm. It can be clearly seen that the fundamental PH modes with mode number of $m$ = 8, 9, 10, 11, 12, 13 disappear one by one when reducing the

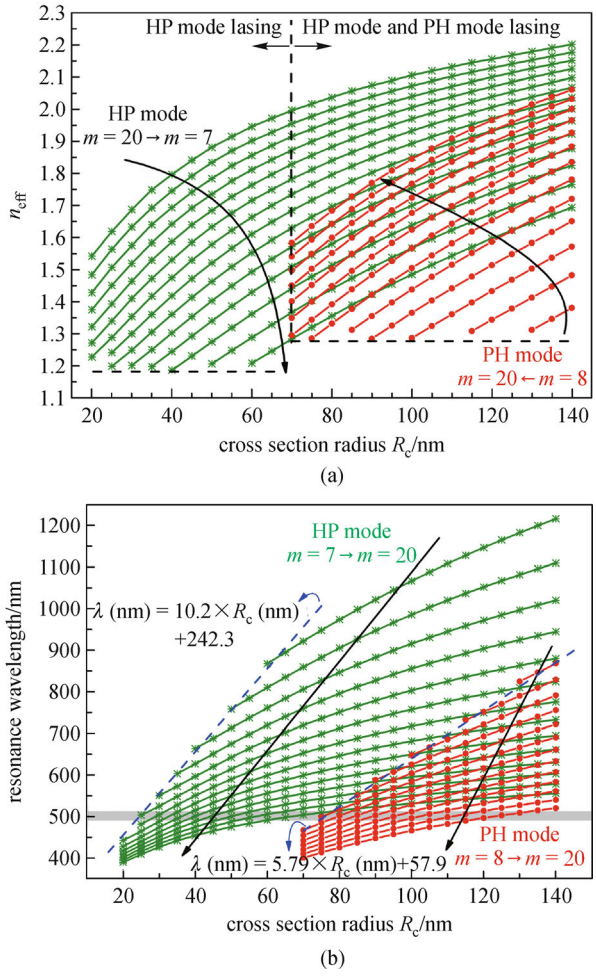


**Fig. 10** Cross section radius ($R_c$) dependence of (a) effective refractive index ($n_{eff}$) and (b) resonance wavelength for the hybrid plasmonic (HP) and fundamental photonic (PH) modes ($H_g$ = 10 nm, $R_r$ = 800 nm) [33]

cross section radius $R_c$ below 130, 115, 100, 90, 85, 75 nm, respectively. In addition, the supported mode number of HP modes becomes $m \geqslant 7$ at $R_c = 60$ nm and $m \geqslant 12$ at $R_c = 25$ nm. Actually, the HP modes with mode number of $m$ = 7, 8, 9, 10, 11, 12 disappear one after another when the cross section radius $R_c$ is reduced below 60, 50, 40, 35, 30, 25 nm, respectively. 5) Although only a limited number of HP modes ($m = 7 \rightarrow m = 20$) and fundamental PH modes ($m = 8 \rightarrow m = 20$) having resonance within the lasing wavelength band is shown in Fig. 10(a), the HP modes with $m < 7$ or $m > 20$ and fundamental PH modes with $m < 8$ or $m > 20$ are also possible in principle. The cross section radius $R_c$ determines the lower limit of mode number of the HP and fundamental PH modes. When reducing the cross section radius $R_c$, the HP and fundamental PH modes with small mode number are cut off gradually. It is shown in Fig. 10(a) that mode number values of $m > 8$ for the fundamental PH modes at $R_c < 130$ nm and $m > 7$ for HP modes at $R_c < 60$ nm are achievable.

The design guidelines of ring resonators to support pure HP modes and choose desired mode number of HP modes are according to critical geometrical dimensions determined by the cut-off phenomenon. Based on the relationship of $2\pi R_r n_{eff} = m\lambda$ between the effective refractive index ($n_{eff}$), mode number ($m$) and resonance wavelength ($\lambda$) for whispering-gallery-like HP and fundamental PH modes, as shown in Fig. 10(b), we further study the cross section radius ($R_c$) dependence of the resonance wavelength for the supported HP and fundamental PH modes. Figure 10(b) presents another straightforward way to find lasing applications for ring resonators. Several important points can be found from Fig. 10(b) as follows. 1) Critical cross section radius ($R_c$) of 70 nm (cut-off of all fundamental PH modes): pure HP modes are achievable when all fundamental PH modes are cut off at $R_c < 70$ nm. 2) Mode number dependence of resonance wavelength: for a given cross section radius ($R_c$), the resonance wavelength decreases with the increase of the mode number. 3) Resonance wavelength range (cut-off of small mode number of HP and fundamental PH modes): $R_c$-dependent lower limit of mode number of the HP and fundamental PH modes is shown in Fig. 10(a). It is noted that there is always a maximum wavelength (upper limit) corresponding to the supported minimum mode number (lower limit) of the HP and fundamental PH modes at a given cross section radius $R_c$. For example, the upper limit resonance wavelength of the HP mode is 440 nm ($m$ = 14) at $R_c$ = 20 nm, 661.6 nm ($m$ = 9) at $R_c$ = 40 nm and 866.3 nm ($m$ = 7) at $R_c$ = 60 nm, as shown in Fig. 10(b). The upper limit resonance wavelength of the fundamental PH mode is 464.3 nm ($m$ = 14) at $R_c$ = 70 nm, 645.6 nm ($m$ = 10) at $R_c$ = 100 nm and 823.2 nm ($m$ = 8) at $R_c$ = 130 nm. Furthermore, two fitting curves for the HP mode ($\lambda(\text{nm}) = 10.2 \times R_c(\text{nm}) + 242.3$) and fundamental PH mode ($\lambda(\text{nm}) = 5.79 \times R_c(\text{nm}) + 57.9$) are deduced, which shows $R_c$-dependent upper limit of the wavelength range (dashed curves in Fig. 10(b)). 4) When taking into account the use of CdS as the gain material for lasing applications, as shown in Fig. 10(b), the possible lasing wavelength band of 489 – 510 nm for CdS is marked in gray bar. It can be clearly seen that a cross section radius ($R_c$) larger than 75 nm is highly desired for possible fundamental PH mode lasing applications (i.e., resonance wavelength is within the gray bar region). Meanwhile, $R_c > 25$ nm is preferred to facilitate potential HP mode lasing applications. To enable pure HP mode lasing applications, the available range of the cross section radius $R_c$ is 25 nm $< R_c <$ 70 nm. In addition, the narrow gray bar region (489 – 510 nm for CdS), as shown in Fig. 10(a), indicates potential single pure HP mode lasing applications. Remarkably, Figs. 10(a) and 10(b) imply a general approach to fully characterize the performance of operation of an active hybrid plasmonic ring resonator for lasing applications, which can be independent of the adopted materials. That is, for different lasing applications using different materials, similar results can be obtained as

shown in Figs. 10(a) and 10(b), indicating critical cross section radius $R_c$ with all fundamental PH modes cut off (i.e., pure HP modes), upper limit of wavelength range (lower limit of mode number) with HP modes possessing small mode number cut off at a given cross section radius $R_c$, and variable range of cross section radius $R_c$ for specific lasing wavelength applications.

It is well known that $Q$ factor and mode volume are two important parameters of a ring resonator, particularly at deep-subwavelength scale. Moreover, for lasing applications using a ring resonator or a ring cavity, a high Purcell factor and a low threshold gain are also desirable [18]. Shown in Figs. 11(a) and 11(b) are $Q$ factor, mode volume, Purcell factor and threshold gain as a function of the ring radius $R_r$ ($H_g$ = 5 nm, $R_c$ = 50 nm). Figure 11(a) depicts the ring radius $R_r$ dependence of the $Q$ factor and mode volume. For simplicity, when taking an ideal case into consideration and ignoring the scattering loss caused by fabrication-induced surface roughness, the total $Q$ factor of the ring resonator ($Q_{total}$) is determined by the radiation loss and material absorption loss following a relationship of $1/Q_{total} = 1/Q_{rad} + 1/Q_{abs}$, where $Q_{rad}$ denotes the weighed impact of radiation loss of the ring resonator, which only considers the geometry-related radiation loss by removing the absorption part of the material; $Q_{abs}$ represents the weighed impact of material absorption loss. As shown in Fig. 11(a), when changing $R_r$ from 300 to 800 nm, a fast increase of $Q_{rad}$ from 250 to 113150 is expected, which indicates that the ring resonator with a relatively larger ring radius $R_r$ features a significant reduction in radiation loss of. It is interesting to find that the total $Q$ factor is dominated by the radiation loss under a small ring radius ($R_r < 400$ nm) while determined by the absorption loss under a large ring radius ($R_r > 400$ nm). Also, a large mode volume is achievable under a large ring radius $R_r$. The mode volume increases from $5.44\times10^{-4}$ to $1.37\times10^{-3}$ μm$^3$ as increasing the ring radius $R_r$ from 300 to 800 nm.

A higher Purcell factor and a lower threshold gain are always highly desirable to facilitate efficient cavity feedback and high efficiency for lasing applications. Shown in Fig. 11(b) is the ring radius $R_r$ dependence of the Purcell factor and threshold gain. Under a ring radius $R_r$ = 400 nm, the highest $Q$ factor together with a relatively small mode volume is obtained as shown in Fig. 11(a), resulting in a maximum value of 813 for the Purcell factor ($F_p$) as shown in Fig. 11(b). For the threshold gain inversely proportional to the $Q$ factor, a minimum value of 1400 cm$^{-1}$ is achieved under a ring radius $R_r$ = 400 nm. It is also found that one can always get a relatively low threshold gain ranging from 1407 to 3187 cm$^{-1}$ as changing the ring radius $R_r$ at submicron size varying from 300 to 800 nm. From the obtained results depicted in Figs. 11(a) and 11(b), it is expected that a compact laser with deep-subwavelength scale, high $Q$ factor, small mode volume, large Purcell factor and low threshold gain might be available by employing an active hybrid plasmonic ring resonator.

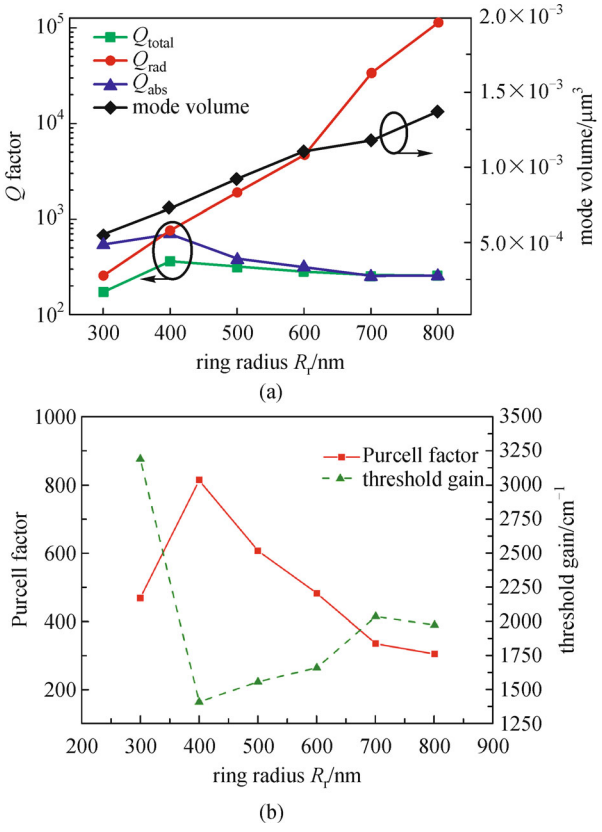


**Fig. 11** Ring radius $R_r$ dependence of (a) $Q_{total}$, $Q_{rad}$, $Q_{abs}$, mode volume and (b) Purcell factor and threshold gain for the HP mode ($H_g$ = 5 nm, $R_c$ = 50 nm) [33]

## 6 Fabricated hybrid plasmonic waveguides [34]

We design and fabricate a vertical hybrid plasmonic waveguide assisted by two tapers for efficient coupling between hybrid plasmonic mode and dielectric mode. Figure 12(a) depicts the schematic structure. Figures 12(b) and 12(c) plot electric field distributions of different hybrid modes under Si waveguide width $W_{Si}$ = 500 nm and $W_{Si}$ = 300 nm, respectively. One can clearly see that narrower Si width benefits efficient confinement of hybrid plasmonic mode in the gap region between Si and Au. Figure 12(d) shows the mode evolution process during the light propagation along the waveguide. The hybrid plasmonic waveguide is fabricated on a silicon-on-insulator (SOI) wafer whose top silicon thickness is 220 nm with 2-μm-thick buried oxide (BOX) layer. The fabrication is carried out in following steps. First, a 220 nm thick Si pattern is generated using electron-beam lithography (EBL) followed by induced coupled plasma (ICP) etching. Then a 220 nm thick gold layer is evaporated on the top of BOX layer close to the Si waveguide by electron beam evaporation after the metal evaporation window is open using EBL overlay technology. Figure 12(e) depicts scanning electron microscopy (SEM) image of a 20-μm

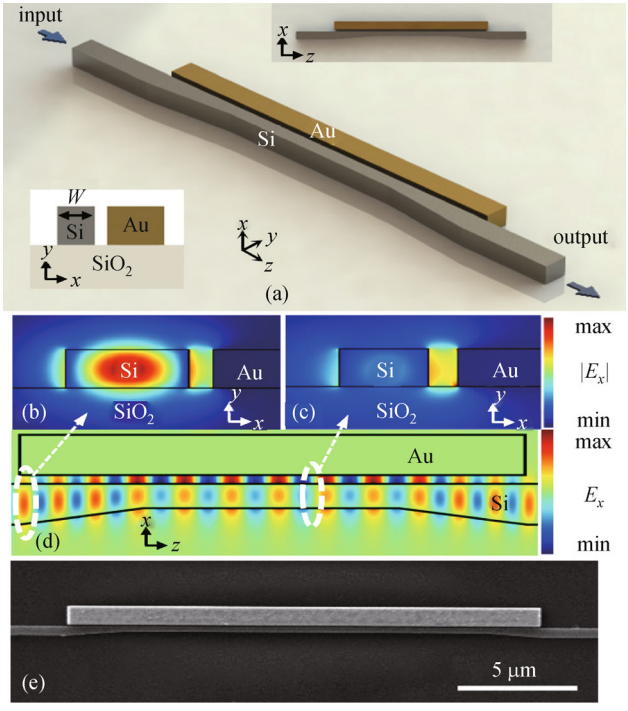


**Fig. 12** (a) Structure of hybrid plasmonic waveguide; electric field distributions in cross section of the waveguide at (b)$W_{Si}$ = 500 nm and (c) $W_{Si}$ = 300 nm, respectively; (d) evolution of electric field distribution propagating along the waveguide; (e) scanning electron microscopy (SEM) image of fabricated hybrid plasmonic waveguide [34]

long hybrid SPP waveguide. We further use the fabricated hybrid plasmonic waveguides for terabit-scale data transmission showing potential use in photonic interconnection. More details of the obtained results and discussion can be found in Ref. [34].

## 7 Broadband generator of orbital angular momentum (OAM) carrying vector beams [35,36]

Phase and polarization are two important properties of electromagnetic waves. Spatial phase or polarization control can create "vortex beams" which have recently attracted increasing interest in a variety of applications. There are two types of vortex beams. One class of vortex beams with phase singularity is featured by a helical phasefront of exp($im\varphi$), where $m$ is topological charge and $\varphi$ is azimuthal angle [53]. Such helical beams carry orbital angular momentum of $m\hbar$ per photon. OAM-carrying vortex beams have seen wide applications in optical manipulation, imaging and optical communications [54–57]. Another class of vortex beams with polarization singularity is characterized by spatially variant polarization of $\alpha(\varphi) = l\varphi + \alpha_0$, where $l$ is the polarization order and $\alpha_0$ is the initial polarization orientation for $\varphi = 0$ [58]. Such vector beams, including widely known examples of radially ($l = 1$, $\alpha_0 = 0$) or azimuthally ($l = 1$, $\alpha_0 = \pi/2$) polarized vector beams, have many applications in optical trapping, spectroscopy and super-resolution microscopy [59]. Furthermore, OAM-carrying vector beams, which combine both "helical" and "vector" features, can give accesses to the spatial phase and polarization and might provide more degrees of freedom for beam manipulation.

We propose and design compact metal-assisted metamaterials to enable broadband generation of OAM-carrying vector beams. Figures 13(a) and 13(b) depict the structure and geometric parameters of metal-assisted metamaterials. We design two concentric rings in a gold film with a thickness of $h$ = 200 nm. Each ring is composed of 42 rectangular apertures with gradually varied orientation. The rectangular aperture array in the gold film can enhance the transmission of linearly polarized light (perpendicular to the aperture direction which might be explained as follows: 1) the localized waveguide resonance (each air aperture can be regarded as a truncated rectangular waveguide with four metal walls and two sides open to air); 2) the property of the surface plasmon resonance due to the aperture array [60,61]. Hence, each rectangular aperture can be regarded as a localized linear polarizer. By controlling the orientation angle of rectangular apertures, we can construct desired spatially variant polarizers to generate OAM-carrying vector beams with right or left circularly polarized input light beam [35]. Figure 13(c) shows an example of phasefront and spatial polarization after passing though the metamaterials, which indicates the generation of OAM-carrying vector beam from circularly polarized beam.

Figure 14 depicts spatial distributions of phase, power and polarization of output beams under the excitation of input left circularly polarized light ($\boldsymbol{E}_{in} = [1\ \mathrm{i}]^T$). We set the wavelength at 1550 nm to characterize the properties of generated OAM-carrying vector beams. The employed metamaterials has an orientation angle of $\alpha(\varphi) = l\varphi + \alpha_0$, where $l$ varies from + 3 to − 3 and $\alpha_0 = 0$. We use $\boldsymbol{E}_1$ and $\boldsymbol{E}_2$ to represent the electric field components along directions of $\boldsymbol{e}_1(\varphi)$ and $\boldsymbol{e}_2(\varphi)$ in Fig. 13(b), respectively. The 1st row of Fig. 14 shows spatial phase distribution of $\boldsymbol{E}_1$, indicating that output beams carry OAM with a charge number of $l$ from + 3 to − 3. The 2nd and 3rd rows of Fig. 14 show spatial power distributions ($P_1 \propto |\boldsymbol{E}_1|^2$, $P_2 \propto |\boldsymbol{E}_2|^2$) along directions of $\boldsymbol{e}_1(\varphi)$ and $\boldsymbol{e}_2(\varphi)$, respectively. It is found that the power component $P_1$ is much larger than $P_2$. The extinction ratio (ER), defined by $10 \times \log_{10}(P_1/P_2)$, exceeds 20 dB. Hence, the electric field component $\boldsymbol{E}_2$ along the direction of $\boldsymbol{e}_2(\varphi)$ can be ignored. The 4th and 5th rows of Fig. 14 show spatial power distributions ($P_x$, $P_y$) along $x$ and $y$ axes, respectively. The alternative bright and dark power distribution implies that the polarization state rotates with the azimuthal angle $\varphi$. The 6th row of Fig. 14 shows calculated spatial polarization distribution, implying the generation of vector beams with a polarization order of $l$ from + 3 to − 3. The obtained results shown in Fig. 14

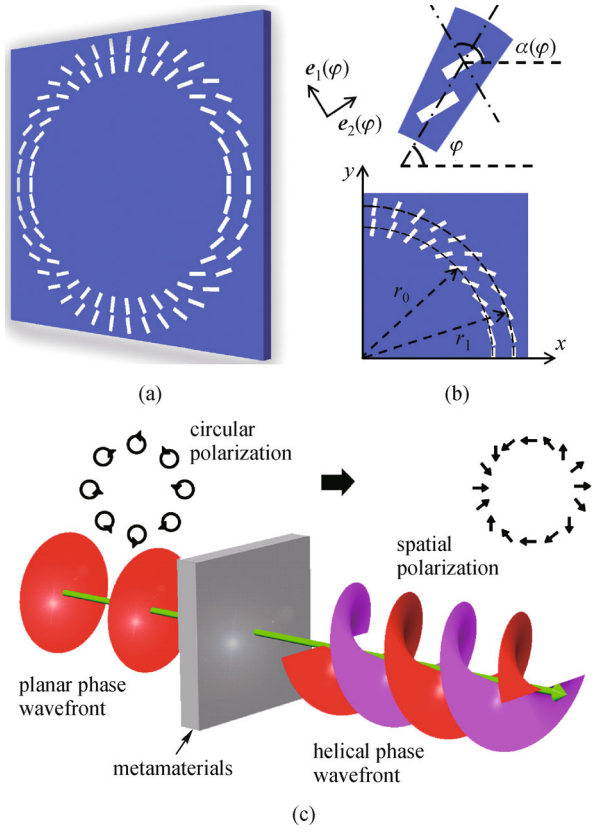


**Fig. 13** (a) Schematic structure of metamaterials for generating orbital angular momentum (OAM)-carrying vector beams; (b) geometric parameters: the radii are $r_i = (i + 6.3) \times 700$ nm ($i = 0$, 1) and the orientation angle is $\alpha(\varphi) = l\varphi + \alpha_0$ ($l = 2$, $\alpha_0 = 0$ as an example) with respect to the $x$ axis. The rectangular aperture has a dimension of 600 nm × 140 nm; (c) illustration of generating OAM-carrying vector beam (OAM charge number: 2, polarization order: 2) [35]

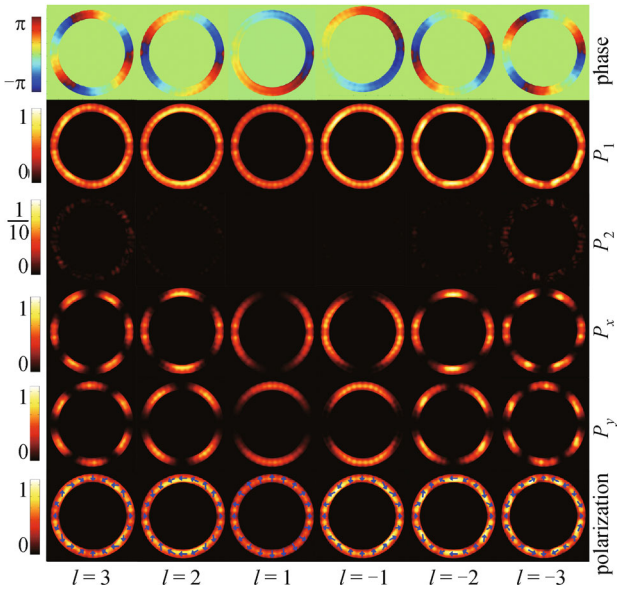


**Fig. 14** Spatial distributions of phase, power and polarization of generated orbital angular momentum (OAM)-carrying vector beams ($\sigma = 1$: left circularly polarized input beam, $\sigma_0 = 0$: along the direction of $\boldsymbol{e}_1(\varphi)$) [35]

confirm the successful generation of OAM-carrying vector beams using metal-assisted metamaterials.

We also study the operation bandwidth. Metamaterials with orientation angle of $\alpha(\varphi) = l\varphi + \alpha_0$ ($l$ = 1,2,3) are considered. Left circularly polarized light is adopted as the input excitation source. We use ER and purity to characterize the quality of the generated OAM-carrying vector beams. Figure 15(a) plots ER as a function of wavelength. One can clearly see the high-quality broadband generation of OAM-carrying vector beams ranging from 1000 to 2500 nm, i.e., from near-infrared to mid-infrared. For $l = 1$ and 2, the ER is kept above 20 dB over a 1500 nm bandwidth (1000 – 2500 nm). For $l = 3$, ER > 16 dB over a bandwidth of 1500 nm (1000 – 2500 nm) and ER > 20 dB over a bandwidth of 800 nm (1000 – 1800 nm) are achieved. Shown in Fig. 15(b) is the wavelength-dependent purity for OAM-carrying vector beam ($l = 3$), which is larger than 0.85 over a bandwidth of 1500 nm (1000 – 2500 nm). The insets depict weight spectra as functions of OAM charge number and polarization order number at 1550 nm. High values of purity are achieved.

In Fig. 13(a), two concentric rings are used to excite a single OAM-carrying vector beam. Actually, one ring can also enable the generation of one OAM-carrying vector beam. Hence, it is possible to generate multiple OAM-carrying vector beams by forming multiple concentric rings in a gold film as shown in Fig. 16, where each ring contains a rectangular aperture array with each aperture acting as a localized polarizer. In particular, it is expected to selectively generate different orders of OAM-carrying vector beams by shining the circularly polarized light source onto different concentric rings.

Figure 17(a) shows ER as a function of wavelength. One can see broadband operation from 1000 to 1550 nm with an extinction ratio above 20 dB, which indicates high-quality broadband (~500 nm) generation of OAM-carrying vector beams. We further study the fabrication tolerance by evaluating the performance dependence on the initial orientation angle $\alpha_{i0}$ of the rectangular aperture. Figure 17 (b) shows the extinction ratio as a function of the initial orientation angle $\alpha_{20}$ of rectangular apertures in the second ring. The extinction ratio is kept above 20 dB when $\alpha_{20}$ is varied from −1° to 7°. The obtained range of initial orientation angle around 8° implies good fabrication tolerance of the designed metamaterials. We use $\boldsymbol{E}_{1i}$ and $\boldsymbol{E}_{2i}$ to denote the electric field components on the directions of $\boldsymbol{e}_{1i}(\varphi)$ and $\boldsymbol{e}_{2i}(\varphi)$ (similar to $\boldsymbol{e}_1(\varphi)$ and $\boldsymbol{e}_2(\varphi)$ in Fig. 13(b)), respectively. We calculate the phase of $\boldsymbol{E}_{1i}$ and the power components on directions of $\boldsymbol{e}_{1i}(\varphi)$, $\boldsymbol{e}_{2i}(\varphi)$, $x$ and $y$ axes, which are presented by $P_1$, $P_2$, $P_x$ and $P_y$, respectively. The spatially variant polarization state of the OAM-carrying vector beams is also calculated. These

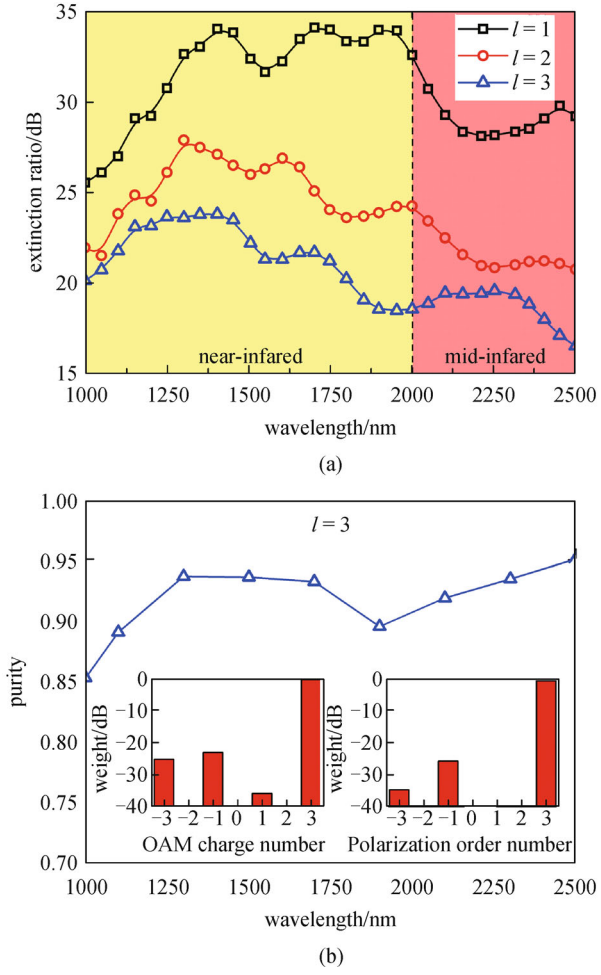


**Fig. 15** Wavelength-dependent (a) extinction ratio (ER) and (b) purity for the generation of orbital angular momentum (OAM)-carrying vector beams. Insets in (b) show weight as functions of OAM charge number (left) and polarization order number (right) at 1550 nm [35]

results are shown in Fig. 17(c). Clearly, the power components on the direction of $\boldsymbol{e}_{1i}(\varphi)$ is much larger than that on the direction of $\boldsymbol{e}_{2i}(\varphi)$. The phase distributions in Fig. 17(c) indicate that the electric field component $\boldsymbol{E}_{1i}$ carries OAM with a charge number of $m = i$ ($i = 1, 2, 3$). Spatial distribution of $P_x$, $P_y$ and the polarization state confirm that the OAM-carrying vector beams have a polarization order of $l = i$ ($i = 1, 2, 3$). More details of the obtained results and discussion can be found in Refs. [35] and [36].

## 8 Conclusions and discussion

In summary, we have reviewed our recent progress in plasmon-assisted nanophotonic devices and applications including LRHPS waveguide, compact plasmonic micro-resonator with efficient thermo-optic tuning, high $Q$ factor and small mode volume, compact active hybrid plasmonic resonator for deep-subwavelength lasing applications, fabricated hybrid plasmonic waveguides for terabit-scale photonic interconnection, and metamaterials-based broadband and selective generation of OAM-carrying vector beams.

For the LRHPS waveguide, the idea comes from both traditional long-range surface plasmon polariton waveguide and hybrid plasmonic waveguide or slot waveguide. It combines both low absorption (long propagation range) property of the long-range surface plasmon polariton waveguide and tight mode confinement property of the hybrid plasmonic waveguide or slot waveguide. These mixed features offer a millimeter-scale propagation range together with a subwavelength mode confinement, which could be used in highly-compact photonic circuits. With future improvement, the LRHPS waveguide can be further optimized along two directions as follows. 1) In addition to

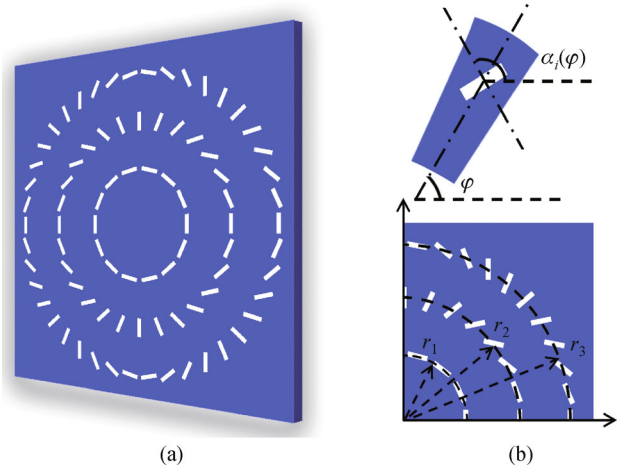


**Fig. 16** (a) Schematic structure of metamaterials; (b) geometric parameters: the radius of the ring is $r_i = (2i + 0.3) \times 700$ nm, where $i = 1$, 2 and 3. The rectangular aperture has dimensions of 600 nm × 140 nm and an orientation angle of $\alpha_i(\varphi) = i\varphi + \alpha_{i0}$ with respect to the $x$ axis [36]

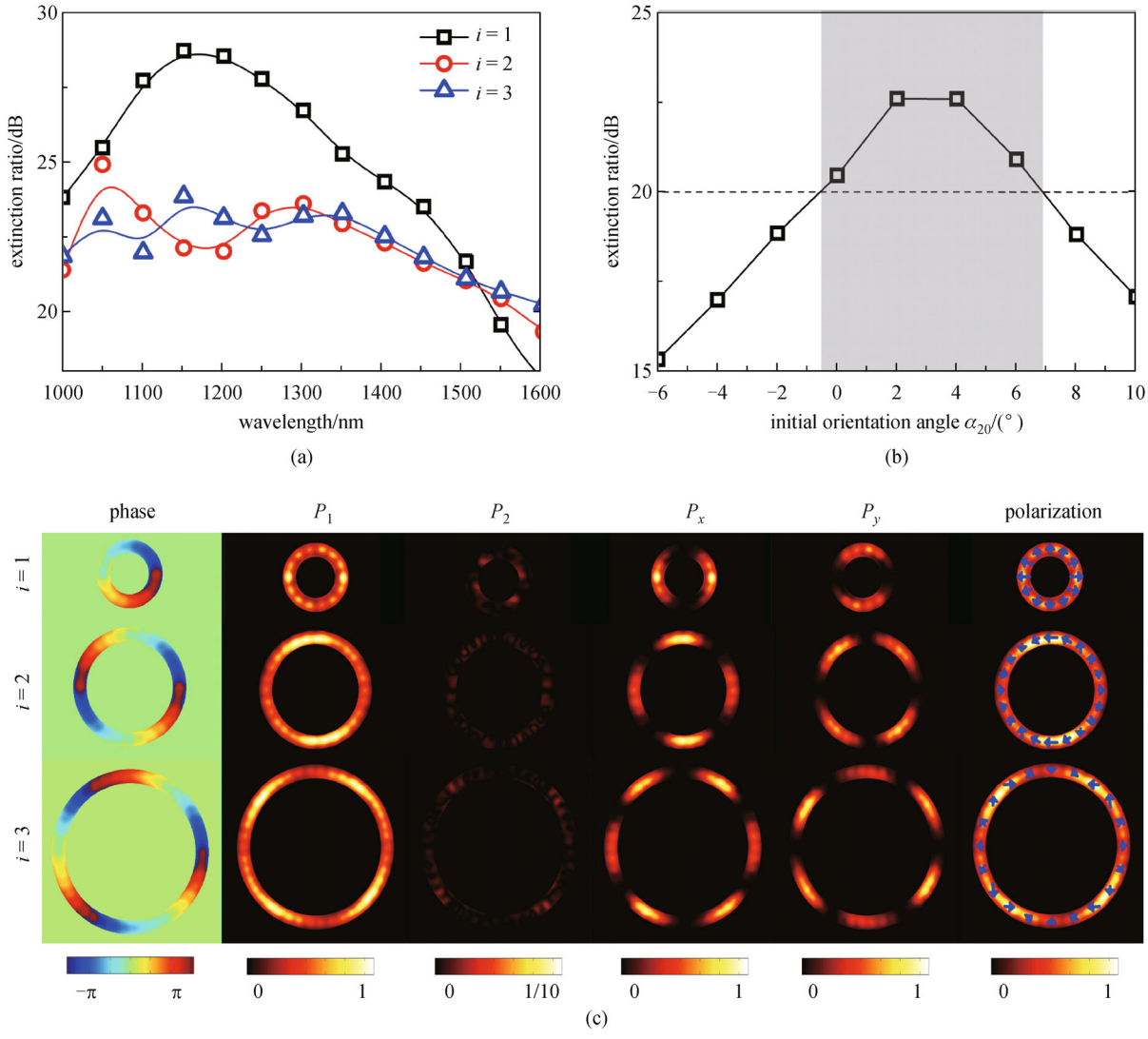


**Fig. 17** (a) Wavelength-dependent extinction ratio for three OAM-carrying vector beams; (b) dependence of extinction ratio on the initial orientation angle $\alpha_{20}$ (second ring); (c) spatial distributions of phase, power components and polarization [36]

Si-nc, some other types of materials can also be used as two slots, depending on different desired material properties. 2) The LRHPS waveguide includes a metal film, two low-index slots and two high-index claddings on a substrate, which provide multiple degrees of freedom to tailor the waveguide geometry. Consequently, the engineering of propagation length, normalized power and intensity, nonlinearity and dispersion is available to fulfill different kinds of applications. For instance, a LRHPS waveguide with high nonlinearity and low chromatic dispersion is beneficial to efficient nonlinear signal processing, such as wideband wavelength conversion based on four-wave mixing, supercontinuum, etc.

For the ultra-compact plasmonic microresonator with efficient thermo-optic tuning, high $Q$ factor and small mode volume, the area of dielectric-metal contact interface is of great importance and depends on the side length of hexagonal shape of ZnO, which could be reduced to ~ 100 nm or smaller while still maintaining a highly confined mode. Additionally, the temperature control for thermo-optic tuning can be fulfilled by various mechanisms (e.g., the electric current induced heating). This type of plasmonic resonator might see potential applications in wavelength-selective on-chip elements, thermal sensing, etc. This microresonator has potential in on-chip components, thermal sensing, and micro/nano-lasing.

For the compact active hybrid plasmonic resonator for deep-subwavelength lasing applications, the designed structure can be further engineered to be applicable for lasing applications at different wavelength bands. Either the high-index nanowire or the low-index gap layer can be considered as the gain medium region, offering more

flexibility to facilitate desired lasing wavelength bands. The available resonance wavelength can be extended in the near-infrared band regardless of lasing wavelength range of gain material. That is, one may choose other appropriate gain materials with specific lasing wavelength range to enable a flexible ring resonator laser operating at desired wavelength band. Benefiting from the round-trip whispering-gallery-like mode properties, the designed active hybrid plasmonic ring resonator structure can avoid the undesired loss due to imperfect reflection at end-facets of previously reported straight plasmon laser structure with Fabry-Pérot-like cavity. Hence, active hybrid plasmonic ring resonator is expected to greatly improve the $Q$ factor. However, how to efficiently collect and output light from the ring resonator appears to be a challenge. Spiral structure could be a possible solution with detailed performance evaluation on the way to be carried out [62]. Moreover, the whole footprint of the proposed active hybrid plasmonic ring resonator is pretty small (submicron size), showing a potential compact lasing solution.

For the fabricated hybrid plasmonic waveguides for terabit-scale photonic interconnection, both high operation speed and ultra-compact dimension are achieved using plasmonic devices, which combines advantages from high-speed photonic devices and nanoscale electronic devices. With future improvement, optimization of structure design and fabrication technique would be expected to further reduce the propagation loss. Hence, longer hybrid plasmonic waveguides with centimeter-scale and bending hybrid plasmonic waveguides might be available to facilitate greatly enhanced flexibility of chip-scale photonic interconnection.

For the metamaterials-based broadband and selective generation of OAM-carrying vector beams, accesses to both spatial phase and polarization of beams offer additional degrees of freedom which might be used in optical communication systems [57]. One could either generate a single OAM-carrying vector beam for a given structure or selectively excite different OAM-carrying vector beams by designing metamaterials with multiple concentric rings in a gold film each containing a self-arranged rectangular aperture array. With further development, relying on similar working principles of local waveguide resonance and surface plasmon resonance, it is possible to fully explore much wider applications with metal-assisted metamaterials, e.g., simultaneous generation and flexible manipulation of multiple OAM-carrying vector beams.

Plasmonics is an exciting new device technology, which exploits the distinct optical properties of metallic nanostructures to facilitate high-speed routing, manipulation and processing at the nanoscale. Although plasmonics bridges photonics and electronics and plasmon-assisted nanophotonic devices feature superior performance in terms of high operation speed and ultra-compact device dimension, it is also highly desirable to promote the compatible-mergence by integrating plasmonic, electronic, and conventional dielectric photonic devices on the same chip and taking full advantage of the strengths of each technology.

**Acknowledgements** This work was supported by the National Natural Science Foundation of China (NSFC) (Grants Nos. 61222502, 61077051, 11274131 and L1222026), the National Basic Research Program of China (973 Program) (No. 2014CB340004), the Program for New Century Excellent Talents in University (NCET-11-0182), the Wuhan Science and Technology Plan Project (No. 2014070404010201), the Fundamental Research Funds of the Central Universities (HUST) (Nos. 2012YQ008 and 2013ZZGH003), and the seed project of Wuhan National Laboratory for Optoelectronics (WNLO).

## References

1. Brongersma M L, Hartman J W, Atwater H H. Plasmonics: electromagnetic energy transfer and switching in nanoparticle chain-arrays below the diffraction limit. MRS Proceedings, 1999, 582: H10.5
2. Zia R, Schuller J A, Chandran A, Brongersma M L. Plasmonics: the next chip-scale technology. Materials Today, 2006, 9(7-8): 20–27
3. Ozbay E. Plasmonics: merging photonics and electronics at nanoscale dimensions. Science, 2006, 311(5758): 189–193
4. Brongersma M L, Shalaev V M. Applied physics. The case for plasmonics. Science, 2010, 328(5977): 440–441
5. Schuller J A, Barnard E S, Cai W, Jun Y C, White J S, Brongersma M L. Plasmonics for extreme light concentration and manipulation. Nature Materials, 2010, 9(3): 193–204
6. Economou E N. Surface plasmons in thin films. Physical Review, 1969, 182(2): 539–554
7. Burke J J, Stegeman G I, Tamir T. Surface-polariton-like waves guided by thin, lossy metal films. Physical Review B: Condensed Matter and Materials Physics, 1986, 33(8): 5186–5201
8. Raether H. Surface Plasmons on Smooth and Rough Surfaces and on Gratings. New York: Springer-Verlag, 1988
9. Barnes W L, Dereux A, Ebbesen T W. Surface plasmon subwavelength optics. Nature, 2003, 424(6950): 824–830
10. Ebbesen T W, Genet C, Bozhevolnyi S I. Surface-plasmon circuitry. Physics Today, 2008, 61(5): 44–50
11. Gramotnev D K, Bozhevolnyi S I. Plasmonics beyond the diffraction limit. Nature Photonics, 2010, 4(2): 83–91
12. Zhang J, Zhang L. Nanostructures for surface plasmons. Advances in Optics and Photonics, 2012, 4(2): 157–321
13. Han Z, Bozhevolnyi S I. Radiation guiding with surface plasmon polaritons. Reports on Progress in Physics, 2013, 76(1): 016402
14. Oulton R F, Bartal G, Pile D F P, Zhang X. Confinement and propagation characteristics of subwavelength plasmonic modes. New Journal of Physics, 2008, 10(10): 105018
15. Alam M Z, Meier J, Aitchison J S, Mojahedi M. Super mode propagation in low index medium. In: Proceedings of Conference on Lasers and Electro-Optics/Quantum Electronics and Laser Science Conference and Photonic Applications Systems Technologies. OSA Technical Digest Series (CD) (Optical Society of America), 2007, JThD112
16. Alam M Z, Aitchison J S, Mojahedi M. A marriage of convenience: hybridization of surface plasmon and dielectric waveguide modes.

Laser & Photonics Reviews, 2014, 8(3): 394–408
17. Oulton R F, Sorger V J, Genov D A, Pile D F P, Zhang X. A hybrid plasmonic waveguide for subwavelength confinement and long-range propagation. Nature Photonics, 2008, 2(8): 496–500
18. Oulton R F, Sorger V J, Zentgraf T, Ma R M, Gladden C, Dai L, Bartal G, Zhang X. Plasmon lasers at deep subwavelength scale. Nature, 2009, 461(7264): 629–632
19. Homola J, Yee S S, Gauglitz G. Surface plasmon resonance sensors. Sensors and Actuators. B, Chemical, 1999, 54(1–2): 3–15
20. Berini P. Long-range surface plasmon polaritons. Advances in Optics and Photonics, 2009, 1(3): 484–588
21. Liu L, Han Z, He S. Novel surface plasmon waveguide for high integration. Optics Express, 2005, 13(17): 6645–6650
22. Dai D, He S. A silicon-based hybrid plasmonic waveguide with a metal cap for a nano-scale light confinement. Optics Express, 2009, 17(19): 16646–16653
23. Dai D, He S. Low-loss hybrid plasmonic waveguide with double low-index nano-slots. Optics Express, 2010, 18(17): 17958–17966
24. Kim J T, Ju J J, Park S, Kim M S, Park S K, Shin S Y. Hybrid plasmonic waveguide for low-loss lightwave guiding. Optics Express, 2010, 18(3): 2808–2813
25. Kwon M S. Metal-insulator-silicon-insulator-metal waveguides compatible with standard CMOS technology. Optics Express, 2011, 19(9): 8379–8393
26. Huang Q, Bao F, He S. Nonlocal effects in a hybrid plasmonic waveguide for nanoscale confinement. Optics Express, 2013, 21(2): 1430–1439
27. Bian Y, Gong Q. Low-loss light transport at the subwavelength scale in silicon nano-slot based symmetric hybrid plasmonic waveguiding schemes. Optics Express, 2013, 21(20): 23907–23920
28. Huang C C. Ultra-long-range symmetric plasmonic waveguide for high-density and compact photonic devices. Optics Express, 2013, 21(24): 29544–29557
29. Chu H S, Li E P, Bai P, Hegde R. Optical performance of single-mode hybrid dielectric-loaded plasmonic waveguide-based components. Applied Physics Letters, 2010, 96(22): 221103
30. Chen L, Zhang T, Li X, Huang W. Novel hybrid plasmonic waveguide consisting of two identical dielectric nanowires symmetrically placed on each side of a thin metal film. Optics Express, 2012, 20(18): 20535–20544
31. Xiang C, Wang J. Long-range hybrid plasmonic slot waveguide. IEEE Photonics Journal, 2013, 5(2): 4800311
32. Xiang C, Wang J, Chan C K. Ultra-compact plasmonic micro-resonator with efficient thermo-optic tuning, high quality factor and small mode volume. In: Proceedings of CLEO: Science and Innovations. Optical Society of America, 2013, JTu4A. 59
33. Xiang C, Chan C K, Wang J. Proposal and numerical study of ultra-compact active hybrid plasmonic resonator for sub-wavelength lasing applications. Scientific Reports, 2014, 4: 3720
34. Du J, Gui C, Li C, Yang Q, Wang J. Design and fabrication of hybrid SPP waveguides for ultrahigh-bandwidth low-penalty 1.8-Tbit/s data transmission (161 WDM 11.2-Gbit/s OFDM 16-QAM). In: Proceedings of CLEO: Applications and Technology. Optical Society of America, 2014, JTh2A. 35
35. Zhao Z, Wang J, Li S, Willner A E. Metamaterials-based broadband generation of orbital angular momentum carrying vector beams. Optics Letters, 2013, 38(6): 932–934
36. Zhao Z, Wang J, Li S, Willner A E. Selective broadband generation of orbital angular momentum carrying vector beams using metamaterials. In: Proceedings of CLEO: QELS Fundamental Science. Optical Society of America, 2013, QM4A. 7
37. Ritchie R H. Plasma losses by fast electrons in thin films. Physical Review, 1957, 106(5): 874–881
38. Almeida V R, Xu Q, Barrios C A, Lipson M. Guiding and confining light in void nanostructure. Optics Letters, 2004, 29(11): 1209–1211
39. Koos C, Vorreau P, Vallaitis T, Dumon P, Bogaerts W, Baets R, Esembeson B, Biaggio I, Michinobu T, Diederich F, Freude W, Leuthold J. All-optical high-speed signal processing with silicon–organic hybrid slot waveguides. Nature Photonics, 2009, 3(4): 216–219
40. Spano R, Galan J V, Sanchis P, Martinez A, Marti J, Pavesi L. Group velocity dispersion in horizontal slot waveguides filled by Si nanocrystals.In: Proceedings of 5th IEEE International Conference on Group IV Photonics. IEEE, 2008, 314–316
41. Berini P. Figures of merit for surface plasmon waveguides. Optics Express, 2006, 14(26): 13030–13042
42. Martínez A, Blasco J, Sanchis P, Galán J V, García-Rupérez J, Jordana E, Gautier P, Lebour Y, Hernández S, Guider R, Daldosso N, Garrido B, Fedeli J M, Pavesi L, Martí J, Spano R. Ultrafast all-optical switching in a silicon-nanocrystal-based silicon slot waveguide at telecom wavelengths. Nano Letters, 2010, 10(4): 1506–1511
43. Vahala K J. Optical microcavities. Nature, 2003, 424(6950): 839–846
44. Oxborrow M. Traceable 2-D finite-element simulation of the whispering-gallery modes of axisymmetric electromagnetic resonators. IEEE Transactions on Microwave Theory and Techniques, 2007, 55(6): 1209–1218
45. Johnson P B, Christy R W. Optical constants of the noble metals. Physical Review B: Condensed Matter and Materials Physics, 1972, 6(12): 4370–4379
46. Bass M, DeCusatis C, Enoch J, Lakshminarayanan V, Li G, MacDonald A, Mahajan V N, Van Stryland E W. Handbook of Optics, Volume II: Design, Fabrication and Testing, Sources and Detectors, Radiometry and Photometry. New York: McGraw-Hill, Inc., 2009
47. Zhang X Y, Hu A, Zhang T, Xue X J, Wen J Z, Duley W W. Subwavelength plasmonic waveguides based on ZnO nanowires and nanotubes: a theoretical study of thermo-optical properties. Applied Physics Letters, 2010, 96(4): 043109
48. Hill M T, Oei Y S, Smalbrugge B, Zhu Y, de Vries T, van Veldhoven P J, van Otten F W M, Eijkemans T J, Turkiewicz J P, de Waardt H, Geluk E J, Kwon S H, Lee Y H, Nötzel R, Smit M K. Lasing in metallic-coated nanocavities. Nature Photonics, 2007, 1 (10): 589–594
49. Noginov M A, Zhu G, Belgrave A M, Bakker R, Shalaev V M, Narimanov E E, Stout S, Herz E, Suteewong T, Wiesner U. Demonstration of a spaser-based nanolaser. Nature, 2009, 460 (7259): 1110–1112
50. Xiao Y F, Li B B, Jiang X, Hu X, Li Y, Gong Q. High quality factor, small mode volume, ring-type plasmonic microresonator on a silver chip. Journal of Physics. B, Atomic, Molecular, and Optical Physics,

2010, 43(3): 035402
51. Zhu L. Modal properties of hybrid plasmonic waveguides for nanolaser applications. IEEE Photonics Technology Letters, 2010, 22(8): 535–537
52. Agarwal R, Barrelet C J, Lieber C M. Lasing in single cadmium sulfide nanowire optical cavities. Nano Letters, 2005, 5(5): 917–920
53. Allen L, Beijersbergen M W, Spreeuw R J C, Woerdman J P. Orbital angular momentum of light and the transformation of Laguerre-Gaussian laser modes. Physical Review A, 1992, 45(11): 8185–8189
54. Franke-Arnold S, Allen L, Padgett M. Advances in optical angular momentum. Laser & Photonics Reviews, 2008, 2(4): 299–313
55. Yao A M, Padgett M J. Orbital angular momentum: origins, behavior and applications. Advances in Optics and Photonics, 2011, 3(2): 161–204
56. Gibson G, Courtial J, Padgett M, Vasnetsov M, Pas'ko V, Barnett S, Franke-Arnold S. Free-space information transfer using light beams carrying orbital angular momentum. Optics Express, 2004, 12(22): 5448–5456
57. Wang J, Yang J Y, Fazal I M, Ahmed N, Yan Y, Huang H, Ren Y, Yue Y, Dolinar S, Tur M, Willner A E. Terabit free-space data transmission employing orbital angular momentum multiplexing. Nature Photonics, 2012, 6(7): 488–496
58. Stalder M, Schadt M. Linearly polarized light with axial symmetry generated by liquid-crystal polarization converters. Optics Letters, 1996, 21(23): 1948–1950
59. Zhan Q. Cylindrical vector beams: from mathematical concepts to applications. Advances in Optics and Photonics, 2009, 1(1): 1–57
60. Ruan Z, Qiu M. Enhanced transmission through periodic arrays of subwavelength holes: the role of localized waveguide resonances. Physical Review Letters, 2006, 96(23): 233901
61. Kang M, Chen J, Gu B, Li Y, Vuong L T, Wang H T. Spatial splitting of spin states in subwavelength metallic microstructures via partial conversion of spin-to-orbital angular momentum. Physical Review A, 2012, 85(3): 035801
62. Poon A W, Luo X, Chen H, Fernandes G E, Chang R K. Microspiral resonators for integrated photonics. Optics and Photonics News, 2008, 19(10): 48–53

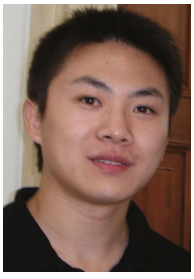

**Jian Wang** (M'12) received the Ph.D. degree in physical electronics from the Wuhan National Laboratory for Optoelectronics, Huazhong University of Science and Technology, Wuhan, China, in 2008. He worked as a Postdoctoral Research Associate in the Department of Electrical Engineering, University of Southern California, Los Angeles, California, USA, from 2009 to 2011. He is currently a professor at the Wuhan National Laboratory for Optoelectronics, Huazhong University of Science and Technology, Wuhan, China. He is the Assistant Director of Wuhan National Laboratory for Optoelectronics. He is also a Chutian Scholar Distinguished Professor in Hubei Province. He gained supports from the New Century Excellent Talents in University in 2011 and China National Funds for Excellent Young Scientists in 2012.

Jian Wang is the member of IEEE, OSA, SPIE and COS. He has more than 150 publications including 2 book chapters, 1 special issue, 2 review articles, 29 invited talks/papers, 6 postdeadline papers, and more than 70 journal papers published on *Science*, *Nature Photonics*, *Scientific Reports*, *Applied Physics Letters*, *Optics Express*, *Optics Letters*, etc. He is a frequent reviewer of *Scientific Reports*, *Optics Express, Optics Letters*, etc. He has devoted his research efforts to photonic integrated devices and high-speed optical communications and optical data processing.